Methods for identifying informative features in agricultural images

Mirzaakbar Hudayberdiev[1], Baxodir Achilov[2], Nurmukhammad Alimkulov[3], Oybek Koraboshev[4], Fakhriddin Abdirazakov[5], Nargiza Sayfullaeva[5]

[1]Department of Software of Information Technologies, Tashkent University of Information Technologies named after Muhammad al-Khwarizmi, Tashkent, Uzbeksitan
[2]Department of Computer Systems, Tashkent University of Information Technologies named after Muhammad al-Khwarizmi, Tashkent, Uzbeksitan
[3]Department of Computer Engineering and Digital Technologies, Kokand University Andijan Branch, Andijan, Uzbekistan
[4]Department of Information Systems and Technologies, Tashkent State Agrarian University, Tashkent, Uzbeksitan
[5]Department of Computer systems, Tashkent University of Information Technologies named after Muhammad al-Khwarizmi, Tashkent, Uzbeksitan

Article Info

Article history:

Received Jun 2, 2025
Revised Sep 20, 2025
Accepted Nov 23, 2025

Keywords:

Fractal dimension
Harris angular measure
Image processing
Informative features
ORB algorithm
Remote sensing

ABSTRACT

The paper deals with informative aspects of images, their scope and extraction methods. The research addresses numerous different types of features such as texture, color, geometric and structural features that play an important role in the field of image analysis and recognition. Contemporary extraction methods based on machine learning algorithms and fractal dimension are explained. The possibility of usage of these methods in real-life problems such as medical imaging, biometrics, remote sensing images processing and agriculture is considered. Successful implementation examples of information functions in real-life problems are presented and opportunities for further research on the topic are considered.

Corresponding Author:

Baxodir Achilov
Department of Computer Systems, Tashkent University of Information Technologies named after Muhammad al-Khwarizmi
Tashkent city, Uzbekistan
Email: borya19861804@gmail.com

1. INTRODUCTION

It needs effective feature extraction techniques that may be employed to recognize, classify, and segment objects within an image [1]. Features play a crucial role in the reduction and acceleration of data processing as well as the improvement of the accuracy of recognition. The importance of this step in the sequence of the process of images cannot be overemphasized since the success of the subsequent steps of analysis largely depends on the quality of the features selected [2]. This paper shall present a class of techniques that may be used to determine the most informative features of an image. Computer vision and image processing continue gaining popularity among many disciplines in the field of science and technology. This paper will discuss the family of methods allowing the determination of the most informative and important characteristics of an image. Computer vision and the processing of images have become popular on a global level in the areas of science and technology [3]. One of the most important steps of the process of the analysis of an image is the definition of informative characteristics, which are compressed and generalized data characterizing the image [4]. Computer vision and the processing of images continue to become popular on a global level in the areas of science and technology. One of the most important steps of the process of the analysis of an image is the extraction of informative characteristics, which are compressed and generalized data characterizing the image [5].

The literature review examines modern image processing techniques, including automated nuclear receptor localization analysis [1], elevation map reconstruction using radar images [2], deep learning for surface debris detection [3], and fire segmentation in drone images [4]. The approaches to improving feature matching [5], classification of diseases in computed tomography (CT) images [6], fractal methods in remote sensing [7], [8], watermark embedding [9], integration of convolutional neural network (CNN) and random sample consensus (RANSAC) for object recognition [10], and other relevant areas in the field of computer vision and image analysis [11]–[20] have been studied.

2. MATERIALS AND METHOD

2.1. Algorithm oriented FAST and rotated BRIEF (ORB) [6]

The methodology proposed in this study involves converting input images into vector representations by extracting key informative features using the ORB algorithm [10]. ORB combines two foundational algorithms: features from accelerated segment test (FAST) for identifying key points, and binary robust independent elementary features (BRIEF) for computing descriptors [21]. The process begins with the detection of informative points across the image using the FAST algorithm. For each candidate pixel, the surrounding 16-pixel circular neighborhood is evaluated to determine whether it constitutes a key point [22]. A pixel is classified as informative if the following condition is met for any subset of contiguous pixels on the circle [11]:

let, $I(p) - p$ be the intensity in pixels. If circle C contains n adjacent sets of pixels, then pixel p is considered the base point.

$$I(p) - I(p_i) > doorstep, \text{ or } I(p_i) - I(p) > doorstep \quad (1)$$

here, p_i is each pixel inside the circle.

The ORB algorithm is designed to transform images into feature vectors, enabling tasks such as object recognition and image matching. This conversion process is structured into four key stages, each building upon the previous one to generate reliable binary descriptors. The overall workflow of the ORB algorithm is depicted in Figure 1. It starts with an input image and moves through the feature detection phase, which leverages the FAST corner detector to efficiently identify potential keypoints. From this initial set, the Harris corner measure is applied to refine the selection, isolating the most stable and distinctive points. After pinpointing these optimal keypoints, the BRIEF descriptor is computed at each location, resulting in a compact and robust binary representation. The end product is a feature vector representation of the image, ready for use in tasks like matching or recognition.

This step-by-step approach enhances ORB's efficiency in real-time applications, leveraging the computational simplicity of both FAST and BRIEF algorithms. Their integration produces a feature descriptor that is not only resistant to noise but also rotation-invariant, making it ideal for diverse computer vision tasks such as object tracking, image stitching, and visual odometry.

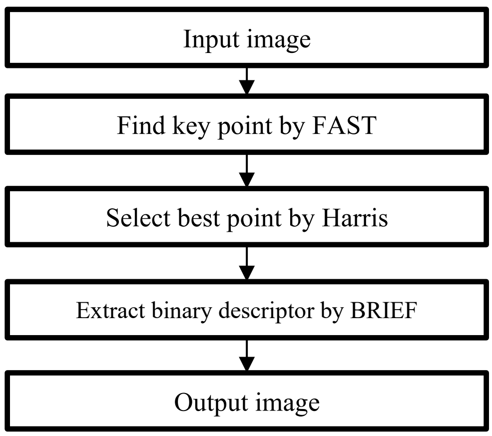

Figure 1. Converting an image to a vector using ORB algorithm

Harris corner measure is used to assess the stability of data points. Harris angular measure is calculated as (2) [12]:

$$R = det(M) - k(trace(M))^2 \tag{2}$$

where, $M -$ gradients are the covariance matrix and a k is a constant (usually between 0.04-0.06). The orientation of the ORB informative gradient points is used to determine the formula (3) [23]:

$$\theta = arctan\left(\frac{\sum_i w_i I(p_i) y_i}{\sum_i w_i I(p_i) x_i}\right) \tag{3}$$

where, w_i is the weight function, and $I(p_i)$ is the pixel intensity.

For descriptor computation, BRIEF performs binary comparisons between pairs of pixels in a smoothed image patch. To ensure rotation invariance, the descriptor coordinates are rotated according to the keypoint orientation [24]:

$$\tau(p, \theta) = (ucos\theta - vsin\theta, usin\theta + vcos\theta), \tag{4}$$

where, τ is the rotating coordinates of the descriptor patch, θ is the orientation of the key point, u and v are the coordinates of pairs of pixels [13].

When generating descriptors, the vector is expressed as a bit string:

$$BRIEF(p) = \sum_{i=1}^{N} 2^{i-1}(I(p) + \tau(u_i, \theta) < I(p) + \tau(v_i, \theta)$$

where, N s the length of the descriptor (for example, 256 bits), I is the pixel intensity, and u_i and v_i are the coordinates of the pixel pairs. ORB descriptors are 32 bits (256 bits) long, each bit is part of a descriptor and represents a texture and other properties around an informative point [25].

2.2. Fractal dimension [7]

Informative features refer to fundamental attributes within an image that carry essential information about its content. These features are critical in tasks such as image recognition, classification, and analysis [14]. In contextual image recognition systems, such features are particularly vital, as their identification enables more effective and accurate image processing [26]. Informative features are widely employed across domains such as agriculture, environmental monitoring, and Earth remote sensing [27].

Some typical informative image features include [15]:

- Edges and borders: The lines, borders, and contours of objects in an image can be important signs of their recognition [16].
- Corners and facet points: Certain points in an image, such as corners, line intersections, or texture nodes, serve as primary markers for highlighting and recognizing objects [17].
- Color properties: Information about the color and color distribution in an image is useful for classifying objects or defining special attributes [18].
- Texture properties: Describing texture properties, such as texture gradients or structural elements, will help in selecting and classifying objects [28].
- Shape and size of objects: Information about the shape, size, and ratio of objects will be important for their identification and classification [19].
- Features of objects: For instance, faces, key points of anatomy, or unique attributes of objects that can be identified in an image [20].

These examples represent a subset of the numerous features that can be extracted for analysis. When various types of features are combined and processed using digital image processing techniques or machine learning models, the accuracy and efficiency of recognition systems can be significantly improved. One such analytical method for structural feature identification is the fractal dimension, which adds an additional layer of spatial complexity to the analysis of image structures [29].

Fractal dimension is a metric used to quantify the complexity or irregularity of a structure, especially in spatially distributed data. In metric spaces, it is used to characterize sets that may not conform to traditional Euclidean dimensions. There are several types of fractal dimensions, including Hausdorff and box-counting dimensions [30]. They are calculated as follows.

Fractal (Hausdorff, box-counting) dimensions are calculated using the formula:

$$d = \lim_{\xi \to 0} \frac{\ln N(\xi)}{\ln\left(\frac{1}{\xi}\right)} \tag{6}$$

where, $N(\xi)$ is the minimum number of cubes with a side of ξ, required to cover the entire complex [31]. The measurement is defined as an exponent of the d degree in $N(\xi)\infty\frac{1}{\xi^d}$ as shown in Figure 2.

- Border block allocation: $N(\xi)\infty\frac{L}{\xi}$,
- Division of total volume blocks: $N(\xi)\infty\frac{L}{\xi^2}$,

Another fractal dimension method is the shoreline method: The length of the coastline is measured in l, then the measured length is calculated using the (7) [32].

$$L = \Delta l^{\alpha}, \Delta = const \tag{7}$$

The box-counting method is implemented through a systematic grid-based measurement technique applied to the target structure. The process is illustrated in Figure 2, which demonstrates the use of the Hausdorff box-counting dimension on a tree structure. In Figure 2(a), the boundary line extraction process is depicted, where the object's contour is transformed into a continuous linear path that represents its geometric complexity for measurement. Figure 2(b) highlights the grid overlay methodology, where boxes of size ε are applied over the structure, and shaded boxes indicate interactions with the boundary, contributing to the count $N(\xi)$. This spatial segmentation enables quantification of how the boundary occupies space at specific resolutions. Figure 2(c) illustrates the iterative refinement through seven stages, progressively increasing grid resolution (decreasing ε) from left to right. The transition in color from red to grayscale portrays the shift toward finer measurement scales, revealing intricate details of the fractal boundary. By plotting $logN(\xi)$ against $log\left(\frac{1}{\xi}\right)$ based on these measurements, the fractal dimension is determined from the slope of the resulting linear graph.

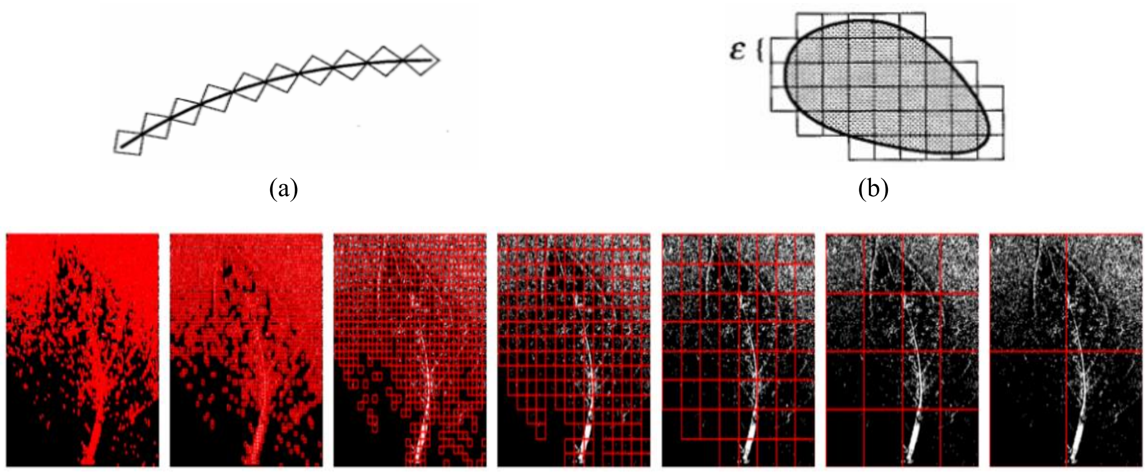

(a) (b)

(c)

Figure 2. Hausdorff box-counting dimension, (a) separation of blocks by boundary line, (b) separation of blocks by total volume, and (c) box-counting

Figure 3 shows traditional ideas about geometry, forms a scale in accordance with predictable, understandable and familiar ideas about the space in which they are located. For example, take a line, divide it into three equal parts, and then each part will be three times less than the length of the original line [33]. It also happens on the plane. If you measure the area of a square and then measure the area of the square by $\frac{1}{\xi}$ the length of the side of the original square, it will be 9 times smaller than the area of the original square. This measurement can be determined mathematically by using the measurement rule according to (8) [34]:

$$N \infty \xi^{-D} \tag{8}$$

where, N is the number of parts, ε is the dimensional coefficient, D is the dimensional coefficient, ∞ is the fractal dimension, which means the proportion in this sign. This scaling rule confirms the traditional rules of geometry scaling, since for a line $N = 3$, when $\xi = \frac{1}{3}$, then $D = 1$, and for squares, because $N = 9$, when $\xi = \frac{1}{3}$, $D = 2$. The same rule applies to fractal geometry, but it is less intuitive. To calculate the unit length of a fractal line, at first glance, reduce the scale three times, in this case $N = 4$, when $\xi = \frac{1}{3}$ and we obtain the value of (8) by changing (9) [35]:

$$\log_{\xi} N = -D \frac{\log N}{\log \xi} \tag{9}$$

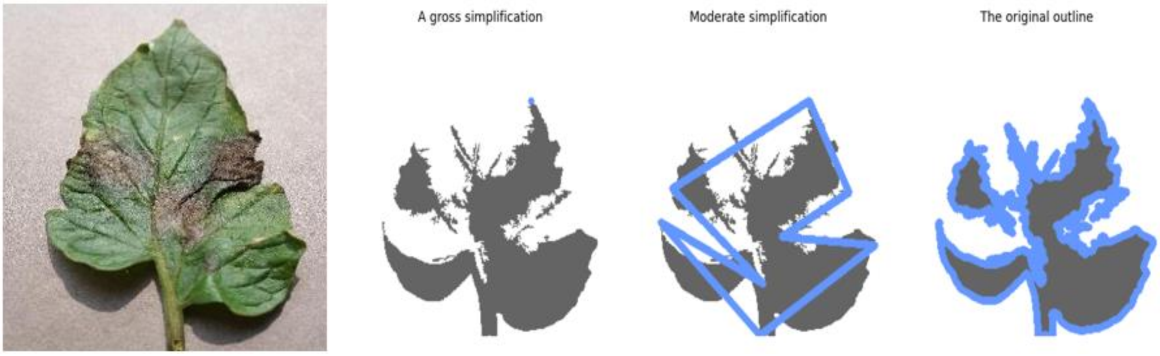

Figure 3. The total length of the coastline

2.3. Normalization signs [8]

Following the extraction of key image features, it is necessary to represent these features in a standardized format suitable for subsequent analysis and classification tasks. This section outlines the process by which object areas and their corresponding informative features are quantified and normalized for consistent use in machine learning pipelines [36]. The following metrics are computed for each image and serve as descriptors of its geometric and structural content:

a. Contrast: A measure of intensity variation across the image.
b. Number of contours ($num\_contours$): Total number of distinct object boundaries detected.
c. Mean contour area ($mean\_contour\_area$): The average area enclosed by identified contours.
d. Standard deviation of contour area ($std\_contour\_area$): Variability in the size of detected regions.
e. Mean contour perimeter ($mean\_contour\_perimeter$): Average length of the perimeters of all contours.
f. Standard deviation of contour perimeter ($std\_contour\_perimeter$): Dispersion in the perimeter lengths.
g. Mean area-to-perimeter ratio ($mean\_area\_to\_perimeter\_ratio$): A shape descriptor capturing object compactness.
h. Fractal dimension: A complexity measure that quantifies the self-similarity or irregularity of the object's shape.

Figure 4 displays the progression of box-counting across three dimensions ($D = 1, D = 2,$ and $D = 3$) over three iteration levels ($l = 1, l = 2,$ and $l = 3$). In the first column ($D = 1$), one-dimensional objects are represented as line segments. At iteration level $l = 1$, there is a single unit line segment with $N = 1$. When subdivided at $l = 2$, the line comprises $N = 2$ segments, and at $l = 3$, N increases to 3 segments, demonstrating a linear relationship where $N = l$. The second column ($D = 2$) depicts square grids in two dimensions. At $l = 1$, the square consists of $N = 1$ unit. This grows to $N = 4$ units at $l = 2$, forming a 2×2 grid, and to $N = 9$ units at $l = 3$, resulting in a 3×3 grid. This scaling follows the relationship $N = l^2$. In the third column ($D = 3$), three-dimensional cubic structures are illustrated. At $l = 1$, there is a single cube ($N = 1$). This count increases to $N = 8$ cubes at $l = 2$, forming a $2 \times 2 \times 2$ configuration, and reaches $N = 27$ cubes at $l = 3$ with a $3 \times 3 \times 3$ configuration. The scaling here follows the formula $N = l^3$. This visualization effectively demonstrates the general scaling law $N = l^D$, which serves as the mathematical basis for calculating fractal dimensions using the box-counting method.

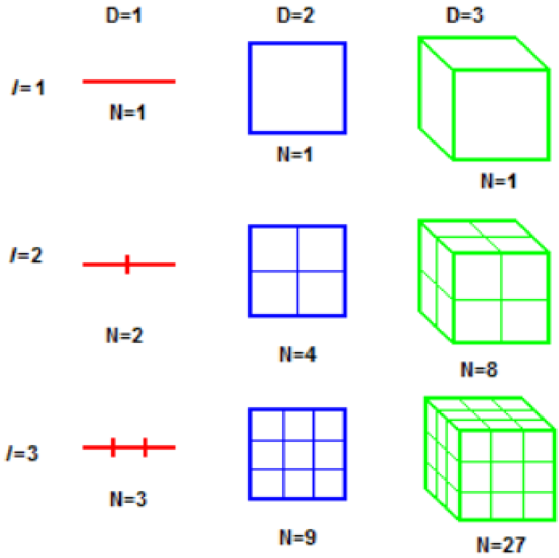

Figure 4. The traditional representation of geometry in measurements and scale determination

The power-law relationship between the number of units and the measurement scale is what sets apart objects of varying dimensionalities and forms the foundation for assessing non-integer fractal dimensions in intricate natural structures. Each of these characteristics corresponds to a feature column in the dataset, representing numerical values that describe an individual image in vector form. These features are critical inputs for classification models, enabling the system to distinguish between image categories based on structural, geometric, and textural patterns.

After identifying informative features, each feature is normalized in the range from 0 to 1 according to formula (10) [37]:

$$I_{i,j}^{normal} = \frac{I_{i,j} - I_{i,j}^{min}}{I_{i,j}^{max} - I_{i,j}^{min}} \tag{10}$$

were, $I_{i,j}^{normal}$ is normalized values, $I_{i,j}$ is input values in the column, $I_{i,j}^{max}$, $I_{i,}^{min}$ minimum and maximum values of the column. By applying this transformation, all feature vectors are scaled uniformly, ensuring that no single feature disproportionately influences the learning process. This step is essential for maintaining model robustness and optimizing classification performance in high-dimensional image datasets.

2.4. Support vector machine [9]

In this study, the support vector machine (SVM) algorithm was employed for the classification of features extracted from images. This machine learning technique was selected due to its high effectiveness in scenarios involving limited training data and its strong generalization capability across diverse datasets. At the initial stage of the classification pipeline, key informative features were extracted from the input images using a combination of ORB feature detection and fractal dimension analysis. These features encapsulated both geometric and textural properties of the target objects. The resulting feature vectors were subsequently normalized, as outlined in section 2.3, and served as input to the SVM classifier.

SVM is a well-established supervised learning algorithm particularly suited for binary classification tasks. The core idea behind SVM is the identification of an optimal separating hyperplane within the feature space that maximizes the margin between data points belonging to different classes. This margin maximization strategy contributes significantly to the model's generalization performance. The SVM operates through the following sequence of steps, enabling effective classification of images based on the extracted features:

2.4.1. Linear support vector machine

Given a labeled training dataset:

$$\{(x_i, y_i)\}, i = 1,2, \dots, n, \ x_i \epsilon \mathbb{R}^d, y_i \epsilon \{-1, +1\} \tag{10}$$

where x_i is a feature vector extracted from an image and y_i is the corresponding class label, SVM seeks to find the optimal separating hyperplane, n is number of training examples [38].
The goal of SVM is to find a hyperplane:

$$w^T x + b = 0 \tag{11}$$

that maximizes the margin between the two classes. The optimization problem is formulated as:

$$\min_{w,b} \frac{1}{2} \|w\|^2 \tag{12}$$

subject to the constraint:

$$y_i(w^T x_i + b) \geq 1, \forall\, i \tag{13}$$

This ensures that all data points are correctly classified with a margin of at least 1. Figure 5 illustration of a linear SVM. The decision boundary separates two data classes and is placed midway between the nearest data points (support vectors). Dashed lines indicate the maximum margin.

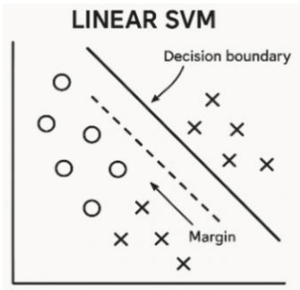

Figure 5. Two-dimensional scatter plot with a linear separating hyperplane of the SVM

2.4.2. Soft margin SVM

In real-world scenarios, perfect separation may not be possible. Therefore, slack variables $\varepsilon_i \geq 0$ are introduced to allow some misclassification. The modified optimization problem becomes [39]:

$$\min_{w,b} \frac{1}{2} \|w\|^2 + C \sum_{i=1}^{n} \varepsilon_i \tag{14}$$

subject to:

$$y_i(w^T x_i + b) \geq 1 - \varepsilon_i,\ \ \varepsilon_i \geq 0 \tag{15}$$

where $C > 0$ is a regularization parameter that controls the trade-off between maximizing the margin and minimizing classification errors. Figure 6 two-dimensional plot illustrating the soft margin SVM, where some data points are allowed within or beyond the margin boundaries.

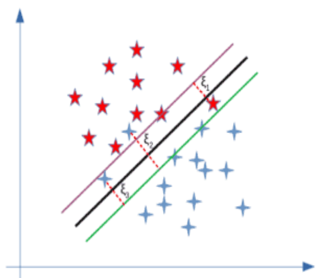

Figure 6. Two-dimensional plot of the support vector machine with a soft margin (soft margin SVM)

2.4.3. Non-linear SVM and kernel trick

When the data is not linearly separable in the original space, a non-linear mapping $\phi(x)$ is applied to project the data into a higher-dimensional feature space where linear separation may be possible. This is efficiently implemented using a kernel function $K(x_i, x_j)$ defined as [40]:

$$K(x_i, x_j) = \phi(x_i)^T \phi(x_j) \tag{16}$$

Common kernel functions include:
- Linear kernel: $K(x_i, x_j) = x_i^T x_j$
- Polynomial kernel: $K(x_i, x_j) = (x_i^T x_j + c)^d$
- Radial basis function (RBF) kernel: $K(x_i, x_j) = \exp\left(-\gamma \|x_i - x_j\|^2\right)$

In this study, the RBF kernel was used due to its ability to handle non-linear feature distributions typical in agricultural image data. Figure 7 visualization of a non-linear SVM using the kernel trick to project data into a higher-dimensional space for linear separation.

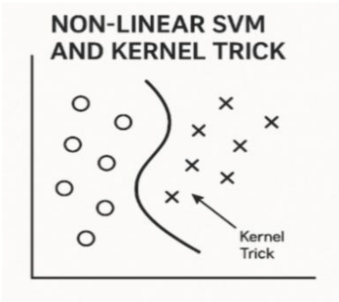

Figure 7. Visualization of a non-linear SVM and the application of the Kernel trick

2.4.4. Decision function

The final decision function used for classification is defined as:

$$f(x) = sign(\sum_{i=1}^{n} \alpha_i y_i K(x_i, x) + b) \tag{17}$$

where α_i are Lagrange multipliers determined during the training phase, and $K(x_i, x)$ computes the similarity between the support vectors and the test input.

The extracted features from the agricultural images—capturing texture, geometric structure, and keypoint-based descriptors—were used to train an SVM model with an RBF kernel. The model parameters C and γ were optimized using k-fold cross-validation to prevent overfitting and ensure generalization. The SVM classifier demonstrated high accuracy and robustness in distinguishing between different image categories based on the informative features. Figure 8 visualization of the SVM decision function and the margin boundaries defined by $f(x) = \pm 1$.

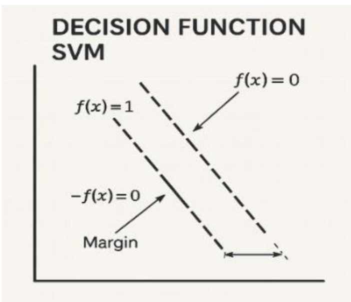

Figure 8. SVM decision function and margin boundaries

2.5. Evaluation metrics

To quantitatively assess the performance of the proposed image classification approach, several standard evaluation metrics were employed. These metrics provide insight into both the overall accuracy and the reliability of the classifier across different categories.

a. Accuracy

Accuracy is the proportion of correctly classified instances among the total number of samples. It is defined as:

$$Accuracy = \frac{TP+TN}{TP+TN+FP+FN} \quad (18)$$

where TP *(True Positives)*: Number of correctly classified positive samples, TN *(True Negatives)*: Number of correctly classified negative samples, FP *(False Positives)*: Number of negative samples incorrectly classified as positive, FN *(False Negatives)*: Number of positive samples incorrectly classified as negative. In this study, the SVM classifier achieved high accuracy in the test dataset, demonstrating high performance in distinguishing image classes based on the extracted informative features.

b. Precision, Recall, and F1-Score

In addition to accuracy, the following metrics were calculated:

– Precision:

$$Precision = \frac{TP}{TP+FP} \quad (19)$$

Measures the proportion of positive identifications that were actually correct.

– Recall (Sensitivity)

$$Recall = \frac{TP}{TP+FN} \quad (20)$$

Measures the proportion of actual positives that were correctly identified.

– F1-Score

$$F1 = 2 \cdot \frac{Precision \cdot Recall}{Precision+Recall} \quad (21)$$

Provides a harmonic mean of precision and recall, especially useful in imbalanced datasets.

c. Cross-validation

To ensure generalizability and avoid overfitting, k-fold cross-validation was performed with $k = 5$. The model maintained stable performance across all folds, indicating its robustness on unseen data.

3. RESULTS

Using the above methods, the results of the study will be as follows. It can be used in several fields, such as remote sensing of the Earth, early detection of diseases by tomato leaves - this, in turn, is a fast and effective result achieved using machine learning. To derive meaningful fractal characteristics from leaf images, a detailed preprocessing and feature extraction pipeline is essential. This multi-step approach processes raw leaf images into precise geometric metrics, which can be utilized for species identification and classification.

Figure 9 outlines the entire workflow for extracting informative features and conducting fractal analysis on a leaf sample. The process starts with Figure 9(a), where a contrast-enhanced binary image isolates the leaf structure from the background, providing a distinct silhouette for further examination. In Figure 9(b), the turn contours representation is displayed, highlighting the traced leaf boundary with key directional changes marked by blue, yellow, and red points connected by lines to emphasize significant geometric properties along the edge. Figure 9(c) demonstrates the calculation of the mean contour area through a vector-based overlay that accounts for the average spatial distribution of boundary features. Similarly, Figure 9(d) quantifies the standard deviation of the contour area, capturing variability in boundary complexity across different parts of the leaf and using a comparable vector notation. The process continues with Figure 9(e), which features the mean contour perimeter measurement, where vectors map characteristic distances along the leaf's edge. In Figure 9(f), the standard deviation of the contour perimeter highlights variations in boundary length across different regions, with denser vector clusters pinpointing areas of high geometric complexity, such as serrated edges. Figure 9(g) showcases the mean area-to-perimeter ratio—a dimensionless metric indicating compactness and irregularity of boundary segments—through spatially distributed measurement vectors. Lastly, Figure 9(h) demonstrates fractal dimension analysis using the box-counting method. Seven iterations with progressively finer grid resolutions (box sizes from 2 to 128 pixels) are presented, illustrating a shift from coarse red grids to fine grayscale grids. Each iteration captures increasingly detailed boundary features, with count values displayed above each grid (ranging from 7 to 311). These values represent a power-law scaling relationship, enabling the computation of the fractal dimension.

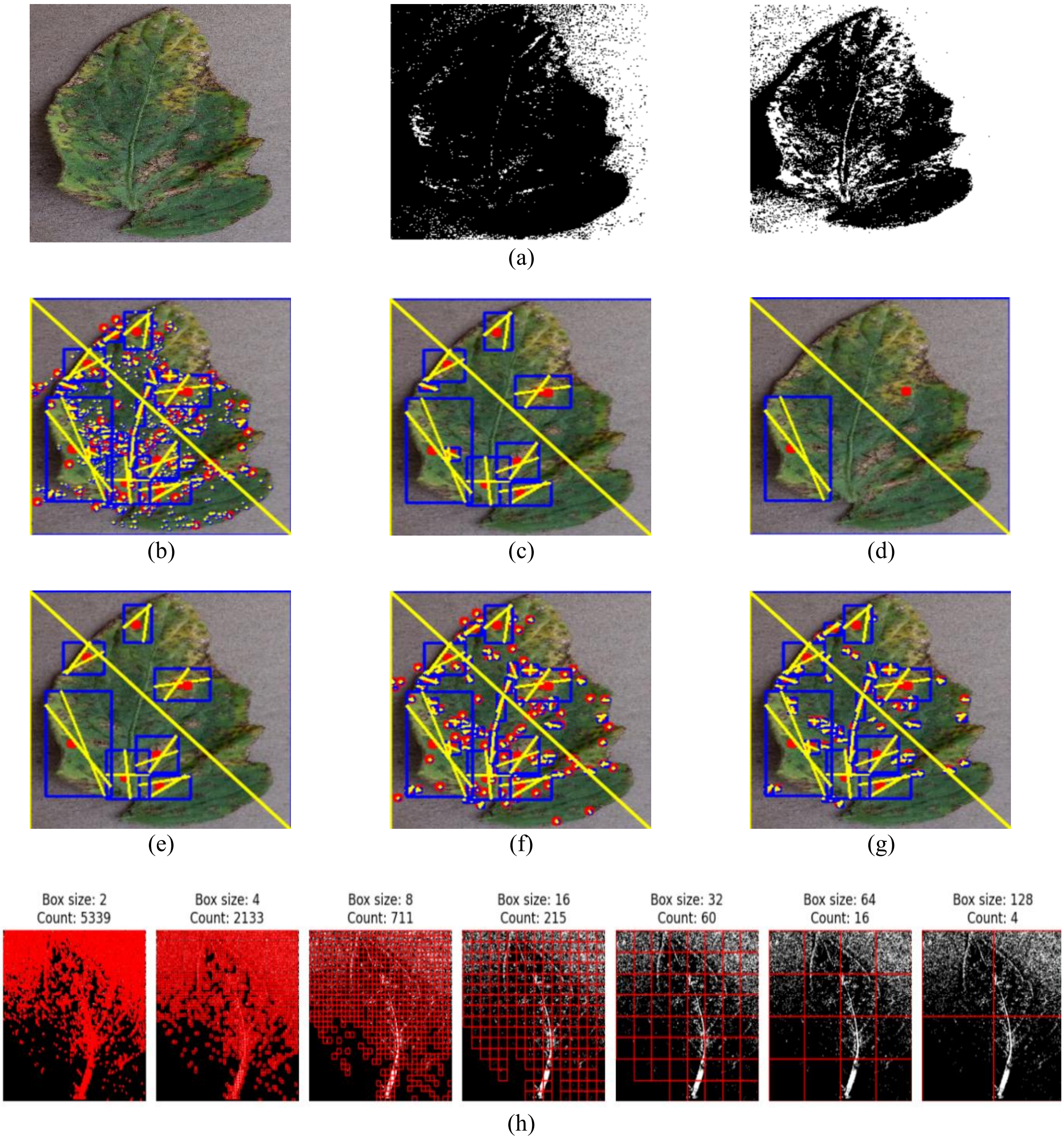

Figure 9. Informative signs, (a) *contrast*, (b) *num_contours*, (c) *mean_contour_area*, (d) *std_contour_area*, (e) *mean_contour_perimeter*, (f) *std_contour_perimeter*, (g) *mean_area_to_perimeter_ratio*, (g) *mean_area_to_perimeter_ratio*, and (h) *fractal_dimension* (box-counting)

This detailed feature extraction method delivers a variety of complementary geometric descriptors that, when integrated, form a reliable signature for identifying leaves. Notably, the fractal dimension measurement provides a scale-invariant representation of boundary complexity, maintaining consistency regardless of changes in viewing distances or image resolutions.

Figure 10 outlines the visualization pipeline used to emphasize key informative features of a leaf specimen. In the left panel, the original image captures a green leaf set against a neutral gray backdrop, showcasing its venation patterns and serrated edges with clarity. Moving to the middle panel, the application of Canny edge detection transforms the leaf into a binary edge map. This step effectively highlights the complete boundary outline and internal vein structures as white lines on a black background, isolating the geometric framework of the leaf. Lastly, the right panel displays the results of ORB keypoints detection, where prominent features are marked on the original image using bright green circles and markers. These keypoints are predominantly located around the serrated edges of the leaf and at intersection points within the venation network, identifying areas of notable geometric intricacy and structural uniqueness. Their spatial arrangement emphasizes that the most significant features arise at points of pronounced curvature changes and texture variation, rather than in the more uniform central regions of the leaf.

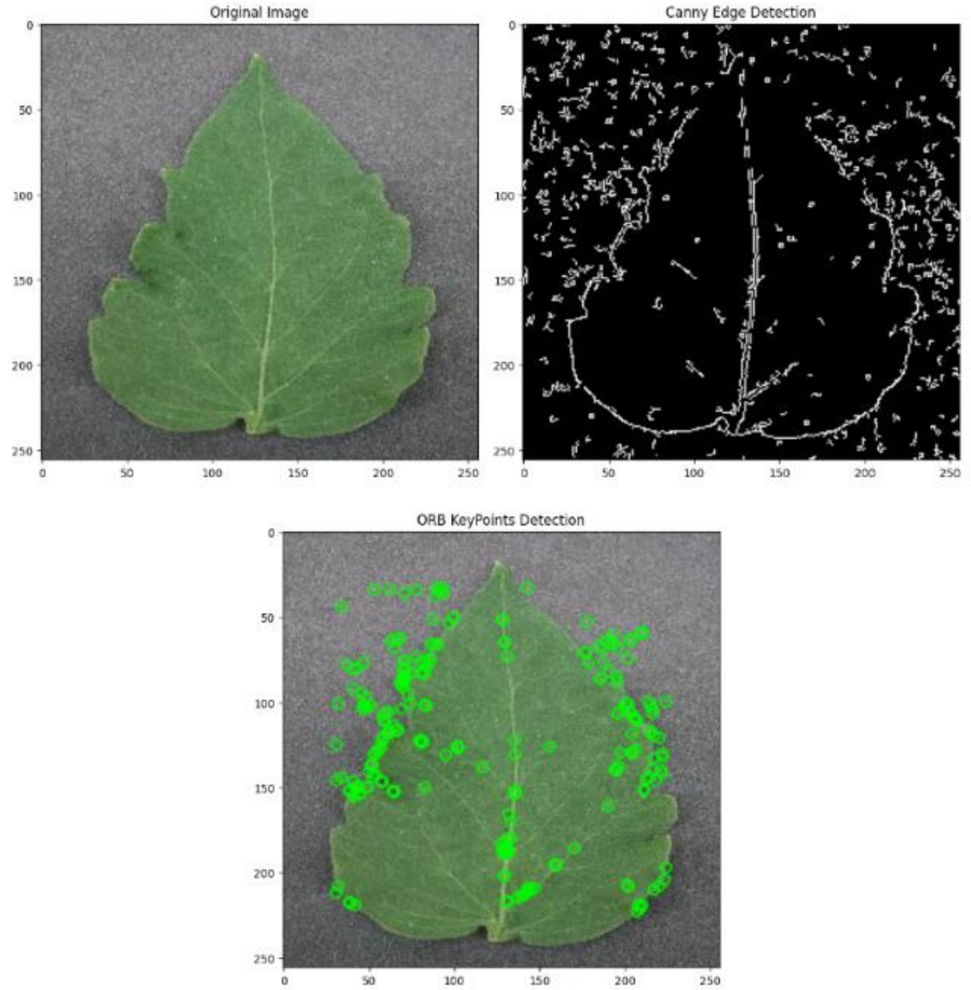

Figure 10. Visualization that highlights informative features

These capabilities allow images to be assessed in terms of their texture, structure, geometric characteristics, and fractal complexity. The resulting data can be used to analyze, classify, or identify patterns in images. Let's consider the results of image research, which are used in several fields when highlighting informative features of an object in an image. A quick and effective result can be obtained with early detection of the disease through tomato leaves. Let's add the above image to the vector representation in the table to facilitate calculations. It can be seen that Table 1 highlights the feature without normalization, and Table 2 highlights it after normalization.

Remote sensing is a method of obtaining information about the Earth's surface and its changes using instruments mounted on satellites, airplanes, or unmanned aerial vehicles. This process involves taking images and measuring various characteristics of the Earth's surface-such as terrain, vegetation, temperature, humidity, and other parameters-without direct physical contact with the object being observed. Remote sensing data is widely used in fields such as agriculture, environmental monitoring, cartography, geology, natural resource management, and emergency response.

The feature extraction methodology, while predominantly demonstrated using botanical specimens, exhibits a versatile application across various domains, including geospatial and remote sensing analysis. The computational techniques, particularly edge detection and keypoint extraction algorithms, prove efficacious for examining intricate natural patterns at diverse spatial scales, spanning from microscopic leaf structures to extensive terrain configurations.

Table 1. Table in the form of vectors before normalization

Classes	contrast	num_contours	mean_contour_area	std_contour_area	mean_contour_perimeter	std_contour_perimeter	mean_area_to_perimeter_ratio	fractal_dimension
Healthy	37.36588247504914	745	41.673154362416106	1096.1588095661043	8.330579827295853	83.11645492742072	0.0698983762629732	1.9015853296688576
Healthy	49.92771511928245	75	799.96	6858.56285225994	45.5727153412501	309.37147289112323	0.3879013626354471	1.9007252278148954
Healthy	44.800203163762916	1070	31.04252336448598	921.8226545107976	11.55998361277803	133.91557719418205	0.05231692861451514	1.9556830542139174
Healthy	35.32940780603492	1242	26.27012882447665	897.8260553703684	6.992370426366871	103.71063206434167	0.032662478234222254	1.9420276684554578
Healthy	36.33191702294344	1291	25.538729666924866	884.1931264970506	6.707476758938442	91.27237081140451	0.03187086575374872	1.9437245964225456
Healthy	51.038177014839626	830	37.859638554216865	1050.186030793863	10.271922461239688	145.63491861360953	0.0476645162238748	1.919027244442953
Healthy	51.80684926493237	507	61.18836291913215	1344.0553293395762	11.741234552460545	125.64160858519503	0.058907243655364615	1.8830814944139642
Healthy	38.43759350132606	1107	28.365853658536587	907.861229755167	6.858337591118714	73.44108053326875	0.04048500480098933	1.9260870754634025
Healthy	39.368361543602774	1240	25.12983870967742	848.3892383064318	6.508126003223081	76.17733156444132	0.038053655871191874	1.9306454133277848
Healthy	38.427830200702935	1107	28.365853658536587	907.861229755167	6.858337591118714	73.44108053326875	0.04048500480098933	1.9260870754634025
First stage	39.273999725351175	1151	27.804083405734143	901.1011957386394	6.915189238344452	71.41015375671913	0.03985761985978902	1.9322419918797769
First stage	52.574191866971965	746	40.35455764075067	1048.1681575750595	12.171922358846537	159.29330957984564	0.05520783542436158	1.9124510072460874
First stage	57.72404060686768	134	199.17910447761193	2290.5429963049346	26.646597888042677	252.77808826862093	0.09643660836105468	1.8154330077924903
First stage	44.605436260083	1061	30.92271442035815	913.9804572898736	11.993313228263819	151.25996205132623	0.052012221871901104	1.9560939503145802
First stage	36.850640038076165	925	35.01945945945946	875.3959500426417	13.16857907900939	73.7731052691163	0.09710209886663952	1.94826502680254
First stage	38.08730485055974	919	34.727965179542984	860.3282270824276	14.263503994075206	88.30024656040648	0.08903344567367813	1.94973927510281
First stage	36.850228013990964	925	35.01945945945946	875.3959500426417	13.16857907900939	73.7731052691163	0.09710209886663952	1.94826502680254
First stage	37.981698385328215	881	36.14755959137344	887.8118660809864	14.588133811409438	93.49671514338834	0.09323897097992496	1.9499467056614945
First stage	48.92713047500953	124	206.52822580645162	2274.7360076380814	16.742698188750975	127.89865018772072	0.19907622373069814	1.7870345881590417
First stage	37.34119746046685	1443	24.1971586971587	867.385794319548	8.667020413417909	101.71834110152199	0.042667114635731494	1.9709397658466221
Second stage	39.10591685280323	1377	25.34495279593319	887.9329218727079	9.792837373571459	127.36523494747124	0.041119528492179015	1.9731529065387348
Second stage	38.883401942783486	1438	23.944367176634213	855.7981179409844	9.0495018621645	100.33991615395894	0.04392614782358721	1.9714532246356589
Second stage	57.75177526008782	678	51.416666666666664	1247.2278748259562	15.822440713556116	180.83996105724125	0.059434476041207156	1.9388854743964816
Second stage	38.72333697675324	214	165.38317757009347	2375.864990617573	26.32458263802751	247.41023763390655	0.10106352566838821	1.8891355810648385
Second stage	61.990945474076625	405	94.4753086419753	1872.7994614606037	18.668592045630938	261.1901641805129	0.05876154472015027	1.9252923799446915
Second stage	48.82860902130554	480	76.35104166666666	1633.1044603246444	16.815952034294604	208.06915011468107	0.07237879742322235	1.926897557527838
Second stage	49.659731961609914	464	78.33728448275862	1630.1568959190565	18.121714001071865	196.44569501262737	0.07936011921240371	1.927572571887288
Second stage	64.78210838493861	200	178.595	2496.7769851300295	21.186206087470055	245.2124320287682	0.09890792559567718	1.8911743632205258
Second stage	65.30879297094319	132	246.93560606060606	2803.6931018053665	25.01716114354856	211.53595109977022	0.17353307346632676	1.8533187558839517
Second stage	38.33655877460931	1092	32.548534798534796	1038.256717694864	8.52881619246888	116.44484812521401	0.046228123066102245	1.9526010944058116

Table 2. Table in the form of vectors after normalization

Classes	contrast	num_contours	mean_contour_area	std_contour_area	mean_contour_perimeter	std_contour_perimeter	mean_area_to_perimeter_ratio	fractal_dimension
Healthy	0.52	0.002	0.019	0.022	0.214	0.002	0.794	0.52
Healthy	0.319	0.005	0.042	0.046	0.326	0.004	0.754	0.319
Healthy	0.267	0.006	0.049	0.032	0.161	0.015	0.701	0.267
Healthy	0.246	0.007	0.052	0.036	0.164	0.016	0.703	0.246
Healthy	0.576	0.002	0.019	0.022	0.218	0.001	0.861	0.576
Healthy	0.349	0.005	0.037	0.038	0.203	0.006	0.777	0.349
Healthy	0.075	0.046	0.231	0.091	0.441	0.021	0.91	0.075
Healthy	0.75	0.001	0.012	0.018	0.126	0.002	0.943	0.75
Healthy	0.118	0.016	0.084	0.104	0.537	0.009	0.5	0.118
Healthy	0.809	0.001	0.009	0.019	0.157	0.002	0.977	0.809
First stage	0.322	0.005	0.046	0.036	0.3	0.006	0.781	0.322
First stage	0.516	0.002	0.012	0.02	0.043	0.006	0.687	0.516
First stage	0.317	0.005	0.041	0.051	0.358	0.005	0.762	0.317
First stage	0.484	0.002	0.013	0.027	0.108	0.005	0.698	0.484
First stage	0.228	0.007	0.042	0.053	0.277	0.009	0.56	0.228
First stage	0.532	0.002	0.023	0.016	0.157	0.003	0.782	0.532
First stage	0.553	0.002	0.016	0.016	0.211	0.001	0.72	0.553
First stage	0.929	0.0	0.0	0.018	0.115	0.002	0.941	0.929
First stage	0.062	0.028	0.116	0.091	0.353	0.023	0.257	0.062
First stage	1.0	0.0	0.0	0.008	0.047	0.0	0.891	1.0
Second stage	0.981	0.0	0.001	0.009	0.058	0.001	0.902	0.981
Second stage	0.71	0.001	0.013	0.029	0.146	0.003	1.0	0.71
Second stage	0.762	0.001	0.008	0.027	0.167	0.002	0.984	0.762
Second stage	0.319	0.005	0.042	0.046	0.326	0.004	0.754	0.319
Second stage	0.406	0.004	0.037	0.047	0.343	0.005	0.92	0.406
Second stage	0.252	0.006	0.034	0.065	0.326	0.011	0.655	0.252
Second stage	0.105	0.031	0.18	0.122	0.552	0.015	0.936	0.105
Second stage	0.075	0.045	0.227	0.124	0.557	0.02	0.951	0.075
Second stage	0.283	0.005	0.016	0.053	0.211	0.009	0.669	0.283
Second stage	0.828	0.001	0.006	0.01	0.017	0.002	0.84	0.828

Figure 11 exemplifies the utilization of the feature extraction pipeline on an earth remote sensing image obtained via satellite. In the leftmost panel, the original image showcases a meandering river system characterized by sinuous curves traversing heterogeneous terrain such as forested areas (denoted by green-brown regions) and water bodies (depicted in blue). This imagery, sourced via Google Earth, serves as a practical case study to assess the robustness of geometric feature extraction algorithms in identifying natural fractal patterns. The middle panel illustrates the application of the Canny edge detection technique, effectively delineating the complex boundaries of the river and surrounding terrain features with white edge outlines against a black background. This outcome highlights the algorithm's capability in tracing the river's intricate meanders and branching patterns, embodying the self-similar characteristics typical of natural waterways.

In the rightmost panel, ORB keypoints detection is represented through bright green markers superimposed on the original satellite image. These markers are predominantly concentrated along the river's course and at branching intersections, pinpointing areas of elevated geometric complexity where structural curvature and directional variations are most prominent. Such findings underscore the efficacy of feature extraction methodologies in providing nuanced insights into the spatial organization of natural systems.

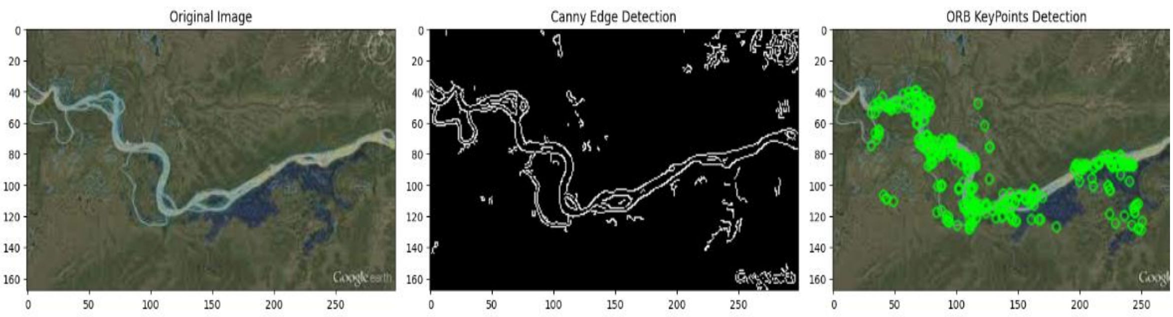

Figure 11. Earth remote sensing image

In Table 3, the selection of features is carried out without normalization, whereas Table 4 shows the results after normalization of the data. The results obtained during the study represent an important stage, given the importance of the informative features of the image. They contribute to achieving high classification accuracy while reducing the time spent on its implementation.

Table 3. Table in the form of vectors before normalization

Classes	contrast	num_contours	mean_contour area	std_contour_area	mean_contour_perimeter	std_contour_perimeter	mean_area_to_perimeter_ratio	fractal_dimension
River	41.579241258787164	356	92.67696629213484	1725.514929536606	13.39729790774624	178.93843721429133	0.06561092475978911	1.884231110988124
River	56.344880469028105	424	76.06721698113208	1391.3985607287061	10.502402803526735	109.87624369138233	0.06799473008265143	1.882831691810061
River	34.45108017051144	807	44.35192069392813	1231.001382376676	6.159621827368991	88.92491196611734	0.044674320714744475	1.9220459938532337
River	23.756907041875834	106	365.1179245283019	3690.835168149927	28.61598781369767	217.13442905071608	0.30046454816201057	1.8762630651870513
River	48.836862005475844	1129	27.232506643046943	856.3461536745542	6.107549364319726	71.96252663718285	0.03404462077599574	1.9210221967360916
River	29.892062869046782	191	167.53403141361255	2271.7122812170646	17.431027398059506	165.12114457696077	0.14271972660807225	1.8643539448644586
River	63.54969862628099	814	36.41707616707617	948.3267863328883	8.7097867037506	72.60089266187208	0.060805650826632286	1.9065475945763684
River	44.89736358550866	930	36.42956989247312	1068.8678696301859	9.070762598770921	122.8510200688499	0.04773615862623374	1.931003767361902
River	49.14369335632184	964	30.929979253112034	868.0745702807158	9.514807352139247	94.42718911101834	0.05300327151522794	1.9237568389445021
River	27.901166235867635	275	119.41636363636364	1915.8601586625298	12.286542994325812	89.9453637012741	0.16882338988968654	1.8720069481494108
Hirhway	24.297871127189143	382	97.09816753926701	1881.0655211725839	12.626819881469167	171.78967303188227	0.08045482259770706	1.9028574353750936
Hirhway	30.175713281400608	514	62.59533073929961	1400.208319220948	10.485181622700004	157.0159388289095	0.05910165107639241	1.8947255665501204
Hirhway	20.757009600171084	113	301.48230088495575	3140.8853212838976	26.215042130082054	182.89159802793318	0.32160021440524045	1.8637593505343975
Hirhway	54.92201371141501	604	52.01158940397351	1223.3443013587835	9.621697483473266	142.00823527656254	0.04014155482530131	1.8989718456210611
Hirhway	59.44748375742923	553	55.53164556962025	1080.829686994994	12.601042580647666	102.99906079962143	0.07953180842282428	1.8990212678125535
Hirhway	43.01092724014021	458	70.15174672489083	1362.974156671575	17.105929515507544	183.29876382125718	0.09104375200685441	1.9075965624867124
Hirhway	63.939397578341016	384	85.2109375	1312.6886674061832	17.439030369122822	135.71559452354566	0.10704124585914597	1.8970132833897535
Hirhway	45.74050714140135	76	277.89473684210526	2377.237781372075	28.241013230461824	186.3268409792821	0.24690430716452835	1.7563395781215114
Hirhway	57.477367984442445	651	48.653609831029186	1058.5206205867694	9.034160144134967	91.6620937275507	0.06539159168850626	1.9010915964546966
Hirhway	25.990904866471766	423	76.81205673758865	1526.2102013626838	11.294508807484421	128.50720224618917	0.06775797271339992	1.880464082498345
AnnualCrop	23.52117889312911	839	38.31883194278903	1084.7764784961537	6.205419281952714	82.9991711390823	0.05463990302945312	1.9045354563684471
AnnualCrop	42.23508876458446	1	10827.5	0.0	866.5067014694214	0.0	12.495575604480305	1.608366167279685
AnnualCrop	43.40537901230686	282	117.49290780141844	1921.2737242136936	15.727409216106361	152.97171815593236	0.10934435175738975	1.876121196082828
AnnualCrop	41.1874677539537	499	63.95190380761523	1365.0943252115703	12.493036177744981	140.61876687049383	0.082268816189977	1.898722879604376
AnnualCrop	28.53161493114735	554	57.234657039711195	1302.6415425040664	9.952087561576375	122.35575509524085	0.06123971034688353	1.891533370851744
AnnualCrop	29.79401777726525	297	120.04882154882155	2031.6796620776508	14.588365733824194	136.33875402526002	0.1125961536477045	1.8759625182737625
AnnualCrop	25.004273458250772	210	154.88809523809525	2214.233396439024	16.01344622032983	164.5120770230593	0.13595647763877985	1.8660296701012185
AnnualCrop	44.20303570389019	908	35.16189427312775	995.8026433018665	7.523445194513262	71.12345634409719	0.04682321850412369	1.916328922102328
AnnualCrop	21.49374346913745	264	130.62310606060606	2081.509554066629	12.154765899434235	129.94880104072072	0.1247717516404765	1.8787910411441144
AnnualCrop	51.116627796838806	904	34.13329646017699	844.259836911002	9.37572674202708	80.34545780024825	0.05932462245757251	1.9200263147467795

Table 4. The table in the form of vectors after normalization

Classes	contrast	num_contours	mean_contour_area	std_contour_area	mean_contour_perimeter	std_contour_perimeter	mean_area_to_perimeter_ratio	fractal_dimension
River	0.448	0.297	0.001	0.053	0.008	0.32	0.001	0.739
River	0.755	0.354	0.001	0.043	0.005	0.197	0.001	0.736
River	0.3	0.675	0.0	0.038	0.001	0.159	0.0	0.825
River	0.078	0.088	0.005	0.114	0.023	0.389	0.004	0.722
River	0.599	0.945	0.0	0.026	0.001	0.129	0.0	0.822
River	0.205	0.159	0.002	0.07	0.012	0.296	0.002	0.695
River	0.905	0.681	0.0	0.029	0.003	0.13	0.001	0.79
River	0.517	0.778	0.0	0.033	0.004	0.22	0.0	0.845
River	0.605	0.807	0.0	0.027	0.004	0.169	0.0	0.829
River	0.164	0.229	0.001	0.059	0.007	0.161	0.002	0.712
Hirhway	0.089	0.319	0.001	0.058	0.007	0.308	0.001	0.781
Hirhway	0.211	0.43	0.001	0.043	0.005	0.281	0.0	0.763
Hirhway	0.015	0.094	0.004	0.097	0.021	0.328	0.005	0.693
Hirhway	0.725	0.505	0.0	0.038	0.004	0.254	0.0	0.773
Hirhway	0.82	0.462	0.0	0.033	0.007	0.184	0.001	0.773
Hirhway	0.478	0.383	0.001	0.042	0.012	0.328	0.001	0.792
Hirhway	0.913	0.321	0.001	0.04	0.012	0.243	0.001	0.768
Hirhway	0.535	0.063	0.004	0.073	0.023	0.334	0.003	0.451
Hirhway	0.779	0.544	0.0	0.033	0.004	0.164	0.001	0.777
Hirhway	0.124	0.353	0.001	0.047	0.006	0.23	0.001	0.731
AnnualCrop	0.073	0.702	0.0	0.033	0.001	0.149	0.0	0.785
AnnualCrop	0.462	0.0	0.166	0.0	0.849	0.0	0.196	0.118
AnnualCrop	0.486	0.235	0.001	0.059	0.01	0.274	0.001	0.721
AnnualCrop	0.44	0.417	0.001	0.042	0.007	0.252	0.001	0.772
AnnualCrop	0.177	0.463	0.0	0.04	0.005	0.219	0.001	0.756
AnnualCrop	0.203	0.248	0.001	0.063	0.009	0.244	0.001	0.721
AnnualCrop	0.103	0.175	0.002	0.068	0.011	0.295	0.002	0.698
AnnualCrop	0.503	0.76	0.0	0.031	0.002	0.127	0.0	0.812
AnnualCrop	0.03	0.22	0.002	0.064	0.007	0.233	0.002	0.727
AnnualCrop	0.646	0.756	0.0	0.026	0.004	0.144	0.0	0.82

Using the informative features of this training sample, we train the SVM algorithm:

a. Illustration of a linear SVM: two groups of points (class -1 in blue and class $+1$ in red) are separated by a decision boundary. The dashed lines represent the margin boundaries $f(x) = \pm 1$. The circled points are the support vectors that define the position of the hyperplane and the width of the margin. Figure 12 Illustration of a linear SVM: two-point classes (−1: blue, +1: red) are separated by a linear decision boundary. Dashed lines represent the margins $f(x) = \pm 1$, and circled support vectors determine the hyperplane and its margin width.
b. Illustration of SVM with an RBF kernel: two groups of points (class −1 in blue and class +1 in red) are separated by a non-linear decision boundary. The shaded regions indicate the classification areas, and the black-outlined circles represent the support vectors that define the shape of the boundary. The RBF kernel function provides an implicit mapping of features into a higher-dimensional space where the classes become separable.

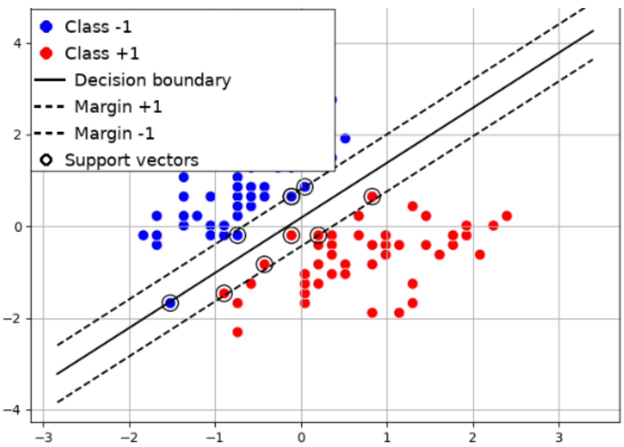

Figure 12. SVM (Linear kernel) with margin equations

Figure 13 shows the SVM with an RBF kernel. Two classes of points (−1: blue, +1: red) are separated by a non-linear decision boundary. Shaded regions represent classification zones, while black-circled points indicate the support vectors that define the shape of the boundary. The RBF kernel enables implicit feature mapping into a higher-dimensional space where the classes become linearly separable.

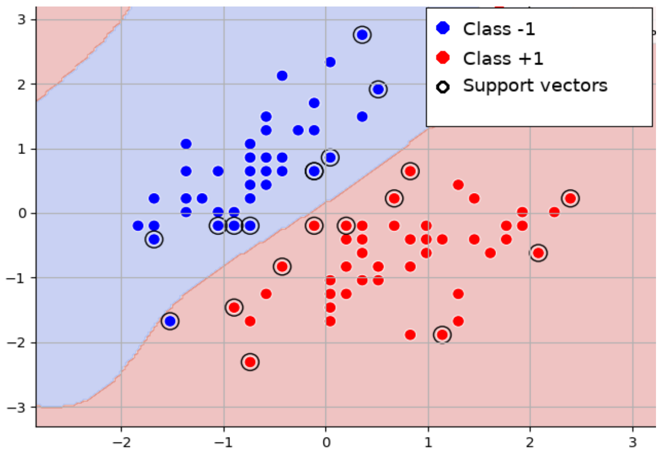

Figure 13. Non-linear SVM classification with RBF kernel

To assess the performance of the classification model, a confusion matrix is utilized to provide a comprehensive analysis of prediction accuracy across all classes. This tool not only highlights the overall accuracy but also uncovers specific misclassification patterns that can guide improvements to the model. Figure 14 illustrates the confusion matrix for the results of the multi-class classification task. The matrix is structured with actual class labels (0 to 4) along the vertical axis and predicted class labels on the horizontal axis. Each cell indicates the sample count, where diagonal cells represent correct classifications, and off-diagonal cells signify errors. The color gradient, ranging from white (indicating zero counts) to dark blue (representing higher counts), offers an intuitive visual representation of classification performance.

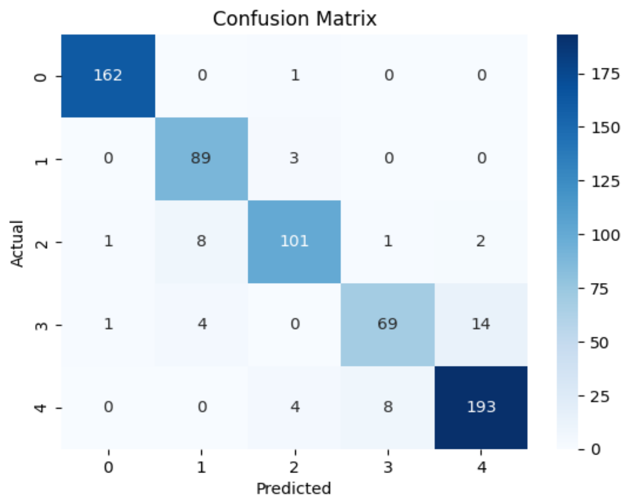

Figure 14. Confusion matrix

Class 0 demonstrates outstanding accuracy, with 162 correctly classified samples and only one misclassified as class 2. Class 1 performs well, achieving 89 correct predictions, though 3 instances were incorrectly assigned to class 2. Class 2 shows solid results with 101 correct classifications, but some challenges are evident—8 samples were misclassified as class 1, 1 as class 3, and 2 as class 4. For class 3, 69 instances were accurately classified; however, there is significant misclassification with 14 samples confused with class 4, alongside a smaller number of errors spread across classes 0, 1, and 2. Finally, class 4 shows the strongest performance, recording 193 correct predictions with minimal errors—4 samples misclassified as class 2 and 8 as class 3.

The experimental evaluation demonstrated that the proposed approach achieved a classification accuracy of 93% with a loss value of 0.07. These results confirm the effectiveness of the applied feature extraction methods combined with the SVM classifier, ensuring both high precision and stability. Such performance highlights the practical applicability of the method for solving real-world image analysis tasks, particularly in the agricultural domain.

Beyond the visualization of the confusion matrix, a detailed classification report offers essential performance metrics for each class, enabling a quantitative evaluation of the model's strengths and weaknesses across various criteria. The classification report associated with Figure 15 provides precision, recall, F1-score, and support values for all five classes (0 through 4).

For Class 0, the performance is outstanding, with precision, recall, and F1-score all at 0.99 across 163 samples. This indicates near-perfect classification with negligible false positives or false negatives. Class 1 exhibits solid results as well, achieving a precision of 0.88 and a recall of 0.97, culminating in an F1-score of 0.92 over 92 samples. While overall strong, this class displays slightly more false positive predictions.

Class 2 delivers balanced performance, reporting a precision of 0.93, a recall of 0.89, and an F1-score of 0.91 for its 113 samples, reflecting relatively equal rates of false positives and false negatives. Conversely, Class 3 fares the weakest, with its precision at 0.88, recall at 0.78, and F1-score at 0.83 across 88 samples. These figures indicate that Class 3 is the most challenging for the model to classify correctly, facing higher confusion with other classes. In contrast, Class 4 demonstrates strong performance consistency, with precision at 0.92, recall at 0.94, and an F1-score of 0.93 across 205 samples, the largest subset, highlighting reliable performance.

When evaluating the overall model performance, an accuracy of 0.93 is achieved over all 661 samples. The macro average—representing unweighted mean scores across all classes—reports precision, recall, and F1-score values of 0.92 each. Meanwhile, the weighted average—which accounts for class imbalances—shows slightly higher values of 0.93 for precision, recall, and F1-score. The improved results in the weighted average suggest that the model performs particularly well on classes with larger sample sizes.

Classification Report:

	precision	recall	f1-score	support
0	0.99	0.99	0.99	163
1	0.88	0.97	0.92	92
2	0.93	0.89	0.91	113
3	0.88	0.78	0.83	88
4	0.92	0.94	0.93	205
accuracy			0.93	661
macro avg	0.92	0.92	0.92	661
weighted avg	0.93	0.93	0.93	661

Figure 15. Classification report

The relationship between model accuracy and loss offers valuable insights into the trade-off between classification performance and prediction confidence. Visualizing these two complementary metrics together allows a better evaluation of whether the model has achieved an optimal balance between accurate predictions and minimal error.

Figure 16 presents model accuracy and loss as interconnected metrics. The horizontal axis is divided into two evaluation criteria: "Accuracy" on the left and "Loss" on the right, while the vertical axis represents metric values, ranging from 0.0 to 1.0. The blue line links the two points, starting at an accuracy value of approximately 0.93 (93%) and declining to a loss value of around 0.07. This inverse relationship is both expected and indicative of a well-trained classification model—high accuracy paired with low loss reflects correct predictions made with strong confidence. The exact values beneath the graph (Accuracy: 0.93, Loss: 0.07) quantify the model's performance, indicating it successfully classifies 93% of test samples while maintaining an error rate of just 7%. The sharp downward slope of the connecting line underscores the pronounced inverse correlation, highlighting that the model has likely reached a stable and effective state.

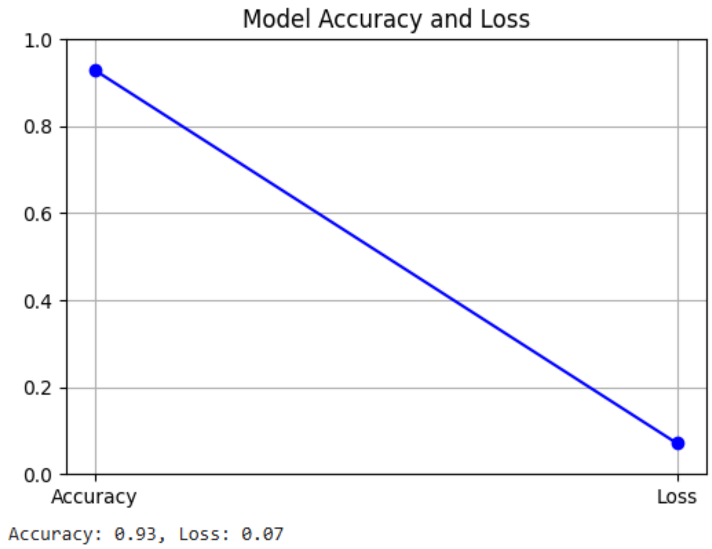

Figure 16. Model accuracy and loss

The observed accuracy-loss relationship demonstrates that the model has been trained efficiently, exhibiting no evidence of overfitting or underfitting. The concurrent presence of high accuracy and low loss values highlights the model's strong generalization ability, reflecting its capacity to produce confident and accurate predictions on the test dataset. These performance indicators are further supported by the detailed analysis provided in the confusion matrix and classification report, which collectively validate the robustness and dependability of the classification system.

4. DISCUSSION

It should be noted separately that the above results were previously used by many researchers in their works and were accompanied by obtaining various results. In particular, a number of scientific publications devoted to the application of machine learning methods in medicine, early detection of diseases from images of leaves, as well as their widespread use in other areas, emphasized that one of the serious problems remains the lack of interpretability of models. This study focuses on short-term feature processing, which plays a key role in achieving high performance. An analysis conducted in another study came to the following conclusions: i) Classification by informative features allows to significantly reduce processing time; and ii) Results are achieved quickly and with high efficiency. However, the reliability that these studies rely on has not been confirmed in our study. Moreover, not only the reliability, but also the universality of the application of the corresponding methods to all machine learning algorithms, not just artificial neural networks, remains questionable.

5. CONCLUSION

This paper introduced the technology of extraction of informative features from images based on the technologies ORB and fractal analysis. Those technologies carry certain advantages and may be effectively used for a wide range of problems. ORB technology guarantees fast and effective detection and description of interest points, which is particularly valuable when there is a necessity to use those applications where there is a requirement for a fast speed of information processing and resistance to rotation of objects. Fractal analysis allows the detection of features due to the geometric nature and the degree of complexity of the structure of the image, which is particularly valuable when there is a necessity to analyze objects having an uneven and complex texture.

Both methods were found to be effective and practical for computer vision and image processing challenges, providing stable and precise outcomes under varied conditions. Experiments on the feature extraction methods such as ORB and fractal analysis confirmed their practicality and real-world applicability. The ORB method was found to be a viable tool for precise and efficient extraction of scale-rotation invariant features. Fractal analysis helped us obtain broad understanding on the nature of images through the analysis of textural characteristics and fractal dimensions. The use of ORB and fractal analysis approaches to informative features extraction demonstrated their strong effectiveness when used in image processing problems. ORB demonstrated an efficient and rapid approach to the detection of keypoints and building the construction of descriptors, which is particularly valuable when dealing with extensive datasets in real time. Fractal analysis opened an invaluable possibility to research the complex and irregular images' structures, opening the deeper insight into their geometric complexity. Thus, the use of both methods opens the gateway towards the continued development of computer vision and computer-driven image processing technologies.

ACKNOWLEDGMENTS

This section should acknowledge individuals who provided personal assistance to the work but do not meet the criteria for authorship, detailing their contributions. It is imperative to obtain consent from all individuals listed in the acknowledgments.

FUNDING INFORMATION

The authors confirm that this research did not receive any external funding and was entirely financed by themselves.

AUTHOR CONTRIBUTIONS STATEMENT

All authors have read and agreed to the published version of the manuscript. Individual contributions according to the CRediT (Contributor Roles Taxonomy) are as follows:

– Mirzaakbar Hudayberdiev: Conceptualization, Methodology, Validation, Formal analysis, Data Curation, Writing – Original Draft.
– Baxodir Achilov: Methodology, Software, Investigation, Writing – Review & Editing, Visualization, Project administration.
– Nurmukhammad Alimkulov: Conceptualization, Formal analysis, Investigation, Resources, Writing – Original Draft.
– Oybek Koraboshev: Software, Validation, Investigation, Data Curation, Writing – Review & Editing, Supervision.
– Fakhriddin Abdirazakov: Methodology, Formal analysis, Resources, Writing – Original Draft, Writing – Review & Editing, Visualization.
– Nargiza Sayfullaeva: Software, Investigation, Writing – Review & Editing, Supervision, Funding acquisition.

Name of Author	C	M	So	Va	Fo	I	R	D	O	E	Vi	Su	P	Fu
Mirzaakbar Hudayberdiev	✓	✓		✓	✓			✓	✓					
Baxodir Achilov		✓	✓			✓				✓	✓		✓	
Nurmukhammad Alimkulov	✓				✓	✓	✓		✓					
Oybek Koraboshev			✓	✓		✓		✓		✓		✓		
Fakhriddin Abdirazakov		✓			✓		✓		✓	✓	✓			
Nargiza Sayfullaeva			✓			✓				✓		✓		✓

C : **C**onceptualization
M : **M**ethodology
So : **So**ftware
Va : **Va**lidation
Fo : **Fo**rmal analysis
I : **I**nvestigation
R : **R**esources
D : **D**ata Curation
O : Writing - **O**riginal Draft
E : Writing - Review & **E**diting
Vi : **Vi**sualization
Su : **Su**pervision
P : **P**roject administration
Fu : **Fu**nding acquisition

CONFLICT OF INTEREST STATEMENT

The authors declare no conflicts of interest. This research was conducted in the absence of any commercial or financial relationships that could be construed as a potential conflict of interest. No funding organizations had any role in the design of the study; in the collection, analyses, or interpretation of data; in the writing of the manuscript; or in the decision to publish the results.

INFORMED CONSENT

We have obtained informed consent from all individuals included in this study. All participants were fully informed about the purpose of the research, the procedures involved, and their right to withdraw at any time. Written consent forms were collected and stored securely in accordance with ethical guidelines and data protection regulations.

ETHICAL APPROVAL

Ethical approval was not required for this study. The research involved only the analysis of leaf specimens and satellite imagery, with no human participants or animal subjects involved in the experimental procedures.

DATA AVAILABILITY

The data that support the findings of this study are not publicly available due to privacy and confidentiality restrictions. Data are available from the authors upon reasonable request and with permission of the appropriate institutional authority.

REFERENCES

[1] L. Bai *et al.*, "Detection of the nuclear translocation of androgen receptor using quantitative and automatic cell imaging analysis," *Tissue and Cell*, vol. 93, p. 102631, 2025, doi: 10.1016/j.tice.2024.102631.

[2] M. Recla and M. Schmitt, "The SAR2Height framework for urban height map reconstruction from single SAR intensity images," *ISPRS Journal of Photogrammetry and Remote Sensing*, vol. 211, pp. 104–120, 2024, doi: 10.1016/j.isprsjprs.2024.03.023.

[3] I. Shad, Z. Zhang, M. Asim, M. Al-Habib, S. A. Chelloug, and A. A. El-Latif, "Deep learning-based image processing framework for efficient surface litter detection in computer vision applications," *Journal of Radiation Research and Applied Sciences*, vol. 18, no. 2, p. 101534, 2025, doi: 10.1016/j.jrras.2025.101534.

[4] B. L. Lawrence and E. de Lemmus, "Using computer vision to classify, locate and segment fire behavior in UAS-captured images," *Science of Remote Sensing*, vol. 10, p. 100167, 2024, doi: 10.1016/j.srs.2024.100167.

[5] X. Jiang, S. Zhang, X. P. Zhang, and J. Ma, "Improving sparse graph attention for feature matching by informative keypoints exploration," *Computer Vision and Image Understanding*, vol. 235, p. 103803, 2023, doi: 10.1016/j.cviu.2023.103803.

[6] N. Alimkulov, S. Ibragimov, B. Achilov, M. Hudayberdiev, and S. J. Khamdamov, "Classification of Lung Cancer risk using digital computed tomography images," in *ACM International Conference Proceeding Series*, 2025, pp. 486–492, doi: 10.1145/3726122.3726192.

[7] M. Khudaiberdiev, I. Khan, B. Tojiboyev, and B. Achilov, "Fractal representations in image processing of remote sensing of the earth," *E3S Web of Conferences*, vol. 541, p. 4010, 2024, doi: 10.1051/e3sconf/202454104010.

[8] K. Dhanda and A. Haynes, "Accumulation points of normalized approximations," *Journal of Number Theory*, vol. 268, pp. 1–38, 2025, doi: 10.1016/j.jnt.2024.09.002.

[9] M. Khudayberdiev, N. Alimkulov, and B. Achilov, "Classification of lung cancer diseases by support vector method (in Russian)," *Science and Innovative Development*, vol. 7, no. 1, pp. 8–20, 2024, doi: 10.36522/2181-9637-2024-1-1.

[10] H. Wang, R. Ma, and P. Niu, "Color image watermarking using vector SNCM-HMT," *Journal of Visual Communication and Image Representation*, vol. 105, p. 104339, 2024, doi: 10.1016/j.jvcir.2024.104339.

[11] X. Zhang, H. Wang, C. Wang, M. Liu, and G. Xu, "Time-segment-wise feature fusion transformer for multi-modal fault diagnosis," *Engineering Applications of Artificial Intelligence*, vol. 138, p. 109358, 2024, doi: 10.1016/j.engappai.2024.109358.

[12] C. N. Öztürk, "An assessment of 2-D and 3-D interest point detectors in volumetric images," *Expert Systems with Applications*, vol. 252, p. 124237, 2024, doi: 10.1016/j.eswa.2024.124237.

[13] D. Bernard, "Polarimetry of γ-rays converting to e+e- pairs with silicon-pixel-based telescopes," *Nuclear Instruments and Methods in Physics Research Section A: Accelerators, Spectrometers, Detectors and Associated Equipment*, vol. 1066, p. 169590, 2024, doi: 10.1016/j.nima.2024.169590.

[14] Y. Tan, H. Xia, and S. Song, "Learning informative and discriminative semantic features for robust facial expression recognition," *Journal of Visual Communication and Image Representation*, vol. 98, p. 104062, 2024, doi: 10.1016/j.jvcir.2024.104062.

[15] M. Cao, Y. Jin, Y. Hu, X. Huang, and J. Wu, "A decision framework for Chinese-style cruise ship design based on informativeness weight method and group consensus reaching model," *Advanced Engineering Informatics*, vol. 62, p. 102698, 2024, doi: 10.1016/j.aei.2024.102698.

[16] C. Prabu V and P. Perumal, "An efficient object detection mechanism with LSTM-based object recognition for computer night vision images in edge and cloud environments," *Applied Soft Computing*, vol. 169, p. 112597, 2025, doi: 10.1016/j.asoc.2024.112597.

[17] Q. Chen *et al.*, "Multi-view 3D reconstruction of seedling using 2D image contour," *Biosystems Engineering*, vol. 243, pp. 130–147, 2024, doi: 10.1016/j.biosystemseng.2024.05.011.

[18] Y. Luo, J. Zhang, and C. Li, "CPIFuse: Toward realistic color and enhanced textures in color polarization image fusion," *Information Fusion*, vol. 120, p. 103111, 2025, doi: 10.1016/j.inffus.2025.103111.

[19] J. Chen, Y. Wang, L. Zhang, and Y. Niu, "Shape reconstruction from focus and image fusion," *Optics and Lasers in Engineering*, vol. 186, p. 108738, 2025, doi: 10.1016/j.optlaseng.2024.108738.

[20] C. Bai, K. Zhang, H. Jin, P. Qian, R. Zhai, and K. Lu, "SFFEF-YOLO: Small object detection network based on fine-grained feature extraction and fusion for unmanned aerial images," *Image and Vision Computing*, vol. 156, p. 105469, 2025, doi: 10.1016/j.imavis.2025.105469.

[21] Y. Xiao, "Integrating CNN and RANSAC for improved object recognition in industrial robotics," *Systems and Soft Computing*, vol. 7, p. 200240, 2025, doi: 10.1016/j.sasc.2025.200240.

[22] S. Pandit, M. A. Kim, J. E. Jung, H. M. Choi, and J. G. Jeon, "Usnic acid brief exposure suppresses cariogenic properties and complexity of Streptococcus mutans biofilms," *Biofilm*, vol. 8, p. 100241, 2024, doi: 10.1016/j.bioflm.2024.100241.

[23] M. W. Ahmed, N. A. Almujally, A. Alazeb, A. Algarni, and J. Park, "Enhanced object detection and classification via multi-method fusion," *Computers, Materials and Continua*, vol. 79, no. 2, pp. 3315–3331, 2024, doi: 10.32604/cmc.2024.046501.

[24] T. Yoshimura *et al.*, "CopDDB: a descriptor database for copolymers and its applications to machine learning," *Electronic supplementary information (ESI)*, vol. 4, no. 1, pp. 195–203, 2024.

[25] B. Zhao, Z. Wang, X. Chen, X. Fang, and Z. Jia, "FApSH: An effective and robust local feature descriptor for 3D registration and object recognition," *Pattern Recognition*, vol. 151, p. 110354, 2024, doi: 10.1016/j.patcog.2024.110354.

[26] G. Zhao, J. Zhu, Q. Jiang, S. Feng, and Z. Wang, "Edge feature enhanced transformer network for RGB and infrared image fusion based object detection," *Infrared Physics & Technology*, vol. 147, p. 105824, 2025, doi: 10.1016/j.infrared.2025.105824.

[27] J. Garrido-Rubio, J. González-Piqueras, A. Calera, and A. Osann, "Remote sensing-based green and blue agricultural water footprint estimation at the river basin scale," *Ecological Indicators*, vol. 167, p. 112643, 2024, doi: 10.1016/j.ecolind.2024.112643.

[28] E. Ropelewska, J. Szwejda-Grzybowska, and M. Mieszczakowska-Frac, "The application of image textures and physicochemical parameters for quality monitoring of freeze-dried cubes and slices of red-fleshed apples," *Journal of Food Composition and Analysis*, vol. 145, p. 107763, 2025, doi: 10.1016/j.jfca.2025.107763.

[29] C. H. P. Rodrigues *et al.*, "Forensic analysis of microtraces using image recognition through machine learning," *Microchemical Journal*, vol. 207, p. 111780, 2024, doi: 10.1016/j.microc.2024.111780.

[30] Y. Yao, C. Du, and L. Xi, "Fractal dimensions of discrete Moran sets," *Chaos, Solitons and Fractals*, vol. 189, p. 115595, 2024, doi: 10.1016/j.chaos.2024.115595.

[31] B. V Prithvi and S. K. Katiyar, "Comments on 'Fractal set of generalized countable partial iterated function system with generalized contractions via partial Hausdorff metric,'" *Topology and its Applications*, vol. 341, p. 108687, 2024, doi: 10.1016/j.topol.2023.108687.

[32] E. B. de Oliveira and E. G. Barboza, "Shoreline change assessment at Arroio do Sal (Southern Brazil) using different shoreline extraction methods," *Remote Sensing Applications: Society and Environment*, vol. 36, p. 101303, 2024, doi: 10.1016/j.rsase.2024.101303.

[33] S. Pandav and S. Kumar Behera, "Circularly polarized 2 × 2 fractal antenna array for space borne tracking applications," *AEU - International Journal of Electronics and Communications*, vol. 178, p. 155249, 2024, doi: 10.1016/j.aeue.2024.155249.

[34] H. Y. Chao, W. T. Li, C. C. Chang, and Y. W. Tsang, "Evaluating the linear accelerator accuracy: Integrating Winston-Lutz measurement method and mathematical calculations," *Radiation Physics and Chemistry*, vol. 217, p. 111504, 2024, doi: 10.1016/j.radphyschem.2023.111504.

[35] S. Kim, I. Jeong, M. Choi, J. Kwak, M. Bencekri, and S. Lee, "Fractal dimensional analysis to reveal traffic flow dynamics as organic metabolism," *Transportmetrica A: Transport Science*, 2024, doi: 10.1080/23249935.2024.2390009.

[36] V. Pitkäkangas, "Rectangular partition for n-dimensional images with arbitrarily shaped rectilinear objects," *Heliyon*, vol. 10, no. 16, p. e35956, 2024, doi: 10.1016/j.heliyon.2024.e35956.

[37] J.-C. Dai, D.-S. Wang, W.-J. Tang, Y.-H. Zou, Y.-X. Hui, and Y.-J. Zhang, "Parameter-normalized probabilistic seismic demand model considering the structural design strength for structural response assessment," *Soil Dynamics and Earthquake Engineering*, vol. 187, p. 109023, 2024, doi: 10.1016/j.soildyn.2024.109023.

[38] S. Chatterjee, S. Pandit, and A. Das, "Coupling of a lightweight model of reduced convolutional autoencoder with linear SVM classifier to detect brain tumours on FPGA," *Expert Systems with Applications*, vol. 290, p. 128444, 2025, doi: 10.1016/j.eswa.2025.128444.

[39] J. Liu, L.-W. Huang, Y.-H. Shao, W.-J. Chen, and C.-N. Li, "A nonlinear kernel SVM classifier via L0/1 soft-margin loss with classification performance," *Journal of Computational and Applied Mathematics*, vol. 437, p. 115471, 2024, doi: 10.1016/j.cam.2023.115471.

[40] I. Zoppis, S. Manzoni, G. Mauri, and R. Dondi, "Kernel machines: support vector machine," in *Encyclopedia of Bioinformatics and Computational Biology*, 2025, pp. 593–600, doi: 10.1016/B978-0-323-95502-7.00120-2.

BIOGRAPHIES OF AUTHORS

Mirzaakbar Hudayberdiev professor (DSc) of the Department of Applied Programming Information Technology, Tashkent University of Information Technologies named after Muhammad al-Khwarazmiy. He earned a degree in mathematics (mathematician and mathematics teacher) from Namangan State University, Uzbekistan, in the 1990s. In 2000, he entered the postgraduate program of the Institute of Informatics of the Academy of Sciences of the Republic of Uzbekistan at the Namangan Institute of Engineering and Economics and received his PhD. In 2007, he defended his diploma in specialty 05.13.18 — "Theoretical foundations of mathematical modeling, numerical methods and software complexes". His thesis topic is "Adaptive models and pattern recognition models in distance learning systems". In 2011-2012, he was awarded an Erasmus Mundus Scholarship from the European Union and conducted doctoral research at the Johannes Kepler University Research Institute for Symbolic Computing in Linz, Austria. In 2022, he received the degree of Doctor of Technical Sciences (D.Sc.) received his degree in the specialty 05.01.03 – "Theoretical foundations of Computer Science" at the Institute for the Development of Digital Technologies and Artificial Intelligence, having defended his thesis on "Optimization procedures for model correction in the algebraic theory of pattern recognition." He can be contacted at email: mirzaakbarhh@gmail.com.

Baxodir Achilov received a bachelor's degree in computer science and information technology from Tashkent University of Information Technology, Samarkand Branch, in 2016 and a Master's degree in computer engineering (Applied programming design) from Tashkent University of Information Technology named after Muhammad al-Khorazmi, Uzbekistan, Tashkent in 2021 and 2023, respectively. Currently, he is a senior lecturer at the Department of Computer Systems, Tashkent University of Information Technology named after Muhammad al-Khorazmi, Tashkent. His research interests include image recognition and artificial intelligence. He can be contacted at email: borya19861804@gmail.com.

Nurmukhammad Alimkulov is an Associate Professor at the Department of Computer Engineering and Digital Technologies, Kokand University Andijan Branch, and holds a PhD in Technical Sciences. Born in 1993 in Andijan region, Republic of Uzbekistan. He successfully completed his Master's degree in information technologies in education in 2019. In 2025, he defended his PhD dissertation in technical sciences on the topic "Algebraic approach algorithms for object recognition in the development of oncoepidemiological intelligent systems." Currently, he conducts scientific research in the fields of pattern recognition, machine learning, and computer vision, with particular focus on the application of artificial intelligence technologies in medicine. He can be contacted at email: alimkulovnurmukhammad@gmail.com.

Oybek Koraboshev received a bachelor's degree in “Informatics and information technologies” from the Tashkent Institute of Architecture and Construction in 2005 and a master's degree in “Applied informatics” from the Tashkent University of Information Technologies named after Muhammad al-Khwarizmi in 2008. Currently, he is a senior lecturer in the Information Systems and Technologies Department of the Tashkent State Agrarian University. He can be contacted at email: koraboshevoybek@gmail.com.

Fakhriddin Abdirazakov In 2016, he earned his master’s degree from the Tashkent University of Information Technologies named after Muhammad al-Khwarizmi. From 2016 to 2023, he served as an Assistant at the Department of Software Support of Information Technologies. In 2023–2024, he held the position of Senior Lecturer in the same department. Since January 3, 2024, he has been pursuing PhD studies at the Department of Computer Systems. His primary research interests lie in the detection of synthetic speech and its differentiation from natural speech, assessment of speech quality and stability, voice signal processing and protection, acoustic and spectral feature analysis, noise reduction techniques, and speaker authentication systems. His work focuses on applying deep learning architectures such as CNN, RNN, LSTM, and Transformer, as well as generative adversarial networks (GANs). He also explores optimization methods including particle swarm optimization (PSO) and genetic algorithms, within the broader framework of artificial intelligence for speech processing applications. He can be contacted at email: boss8388@mail.ru.

Nargiza Sayfullaeva a bachelor's degree in computer science and information technology from the Tashkent University of Information Technology (Uzbekistan) in 2010, as well as a master's degree in hardware and software for biotechnical systems from the Tashkent University of Information Technologies (Uzbekistan) in 2012, respectively. Currently an Acting Associate Professor in the Computer Systems Department at the Tashkent University of Information Technologies named after Muhammad al-Khwarizmi. Her research interests include computer science, artificial intelligence, the use of big data technology in hydrogeological research, and cartographic data used in GIS. She can be contacted at email: sayfullaeva@tuit.uz.